The Astrophysical Journal, 722:1290–1302, 2010 October 20 doi:10.1088/0004-637X/722/2/1290

TRANS-NEPTUNIAN OBJECTS WITH *HUBBLE SPACE TELESCOPE* ACS/WFC*

Cesar I. Fuentes[1,2], Matthew J. Holman[1], David E. Trilling[2], and Pavlos Protopapas[1]
[1] Harvard-Smithsonian Center for Astrophysics, 60 Garden Street, Cambridge, MA 02138, USA; cfuentes@cfa.harvard.edu
[2] Department of Physics and Astronomy, Northern Arizona University, P.O. Box 6010, Flagstaff, AZ 86011, USA
Received 2010 May 9; accepted 2010 August 10; published 2010 September 29

ABSTRACT

We introduce a novel search technique that can identify trans-Neptunian objects in three to five exposures of a pointing within a single *Hubble Space Telescope* (*HST*) orbit. The process is fast enough to allow the discovery of candidates soon after the data are available. This allows sufficient time to schedule follow-up observations with *HST* within a month. We report the discovery of 14 slow-moving objects found within 5° of the ecliptic in archival data taken with the Wide Field Channel of the Advanced Camera for Surveys. The luminosity function of these objects is consistent with previous ground-based and space-based results. We show evidence that the size distribution of both high and low inclination populations is similar for objects smaller than 100 km, as expected from collisional evolution models, while their size distribution differs for brighter objects. We suggest that the two populations formed in different parts of the protoplanetary disk and after being dynamically mixed have collisionally evolved together. Among the objects discovered there is an equal-mass binary with an angular separation ∼0.″53.

Key words: celestial mechanics – Kuiper Belt: general – methods: observational – planets and satellites: formation – surveys

Online-only material: color figures

1. INTRODUCTION

Trans-Neptunian objects (TNOs) represent the leftovers of the same planetesimals from which the planets in the solar system formed. These offer a unique opportunity for testing theories of the growth and collisional history of planetesimals and the dynamical evolution of the giant planets (Kenyon & Bromley 2004; Morbidelli et al. 2008). The study of the orbital distribution of TNOs has shown the existence of at least two distinct dynamical populations (Levison & Stern 2001; Brown 2001) with different colors (Doressoundiram et al. 2008) and size distributions (Bernstein et al. 2004; Fuentes & Holman 2008).

Most of what is known about TNOs is based on follow-up studies of the brightest objects (Brown 2008). The bias toward analysis of brighter objects can be seen in challenging observations like light curves and binarity fraction. This is even more apparent for spectroscopic observations and albedo measurements, which are available for only ∼30 objects (Stansberry et al. 2008; Brucker et al. 2009), among which the smallest is over 130 kmin diameter. This is explained by the relative faintness of outer solar system bodies and the difficulty of tracking them after discovery. Observations made several months and even years apart are needed to secure accurate orbits. In general, the fainter the object the more demanding the observing conditions necessary to detect and track it.

Despite the challenge, a great deal of effort has been dedicated to searching for faint TNOs (Chiang & Brown 1999; Gladman et al. 2001; Allen et al. 2002; Bernstein et al. 2004; Petit et al. 2006; Fraser et al. 2008; Fuentes & Holman 2008; Fraser & Kavelaars 2009; Fuentes et al. 2009). These surveys have concentrated near the ecliptic, where the sky plane density of objects is largest. Elaborate observational techniques have been developed to extend the sensitivity of these surveys. Usually, a compromise is reached between the sky coverage and magnitude depth of these resource intensive techniques. This results in "pencil beam" searches that concentrate on a limited region of the sky. The results produced are statistically calibrated and provide a precise assessment of the TNO sky plane density. However, these surveys typically obtain short arcs, yielding imprecise information about TNO orbits.

These studies have extended our understanding of the TNO size distribution to tens of km in diameter. In the deepest survey to date, reaching a limit of $R \sim 28.5$, Bernstein et al. (2004) recognized a break using *Hubble Space Telescope* (*HST*) data at $R \sim 25$. Bernstein et al. (2004) was consistent with the results of other surveys that were only sensitive to bright objects. However, those searches claimed that the luminosity function of bright objects could be extended up to a magnitude $R \sim 26$ (Gladman et al. 2001; Petit et al. 2006). The controversy was settled when Fuentes & Holman (2008) corroborated the existence of the break. That work had the advantage of being a single survey with the sky coverage and magnitude depth to be sensitive to $R \sim 25.5$ objects and obtained a statistically significant result that did not rely on the combination of fields observed under various conditions. Deeper ground-based searches have been able to narrow the gap between ground- and space-based surveys by co-adding data taken over an entire night (Fraser & Kavelaars 2009; Fuentes et al. 2009).

Brown (2001) determined that the TNO inclination distribution was well fit by the sum of a narrow and wide Gaussian distribution. Bernstein et al. (2004) used the somewhat arbitrary value of $i = 5°$ to differentiate between hot and cold objects and recognized different size distributions for both populations. They determined the size distribution of hot objects had a shallower slope than that of cold objects for objects larger and smaller than the break. Observationally, most large objects are hot and most small objects are cold. However, this result was

* Based on observations made with the NASA/ESA *Hubble Space Telescope*, obtained from the Data Archive at the Space Telescope Science Institute, which is operated by the Association of Universities for Research in Astronomy, Inc., under NASA contract NAS 5-26555. These observations are associated with program 11778.

based on a few objects smaller than the break, especially on the three cold TNOs found by Bernstein et al. (2004).

A simple definition for hot and cold objects is useful for pencil beam surveys where the constraint on the orbits is not precise. From the ground not much more than a rate of motion on the sky is obtained from a night's worth of observation. The large uncertainties associated with the distance and inclination estimated under the assumption of a circular orbit could eventually bias the analysis. A survey able to find faint objects ($R \sim 26$) and provide accurate constrains on the distance and inclination could show if indeed there is a difference in the size distribution of high and low inclination objects.

The most basic information that can be extracted from a set of TNO discoveries is the luminosity function. If the albedo is assumed and the distance to each object can be estimated, the size distribution is obtained. With further information about the trajectory of an object, we can estimate its inclination, which can be used as a proxy for dynamical excitation. Ground-based detections provide a very short arc that gives us limited information about the distance if the degeneracy between the object's velocity and parallactic motion cannot be disentangled.

The *HST* has the advantage of not being affected by atmospheric seeing, achieving very precise astrometric measurements. Also, its orbital motion about the Earth adds extra parallax to the observations. For solar system bodies, this helps in unraveling the contributions of the Earth's parallax and the object's intrinsic motion, allowing precise orbital estimates, even when not observing at opposition.

The objective of our investigation was to find faint TNOs with acceptable orbital uncertainties to further constrain the size distribution of the hot and cold populations. For this we defined a limited, well-characterized search for moving objects. Our search is sensitive to $R \sim 26$ and is able to constrain the distance and inclination of the objects discovered. In Section 2, we present a summary of the data selection and acquisition. The characterization of the search algorithm is done by sampling a control population, described in Section 3. The detection pipeline is described in detail in Section 4, and the detection efficiency is explained in Section 5. Results and analysis of the data appear in Section 6, where special emphasis is given to testing the capabilities of *HST* in finding the correct orbital information. We discuss the significance of our findings in Section 7. Our conclusions are presented in Section 8.

2. DATA

Objects in the TNO realm (∼42 AU) exhibit parallactic motion of $\sim 3'' h^{-1}$ when observed at opposition, mainly due to Earth's translation. Depending on the resolution and data quality of the observations, TNOs are readily identified by this motion if two or more images of the same field are taken with an adequate interval between exposures. This parallactic motion implies that if the shutter is kept open for a time longer than it takes a TNO to move beyond its point-spread function (PSF), the image will trail. If observed at opposition, an image of a typical TNO will take ∼10 minutes to traverse the PSF of a ground-based image (FWHM $\sim 0\farcs5$) while only 1 minute in an image is taken with the Wide Field Channel of the Advanced Camera for Surveys (ACS/WFC, FWHM $\sim 0\farcs05$).

We focused our search on data taken with ACS/WFC, the largest field of view camera on *HST* ($202'' \times 202''$ or 0.003 deg^2). Bernstein et al. (2004) co-added tens of ACS/WFC exposures to reach a sensitivity of $R \sim 28.5$. However, of the three objects they discovered two of them were detected in each individual image, and the faintest ($R = 27.8$) exhibited a light curve that made it visible in a fraction of the exposures. The latest results for the TNO luminosity function (Fuentes et al. 2009; Fraser & Kavelaars 2009) indicate that the sky density of TNOs brighter than $R = 27$ on the ecliptic is 0.5 per ACS/WFC field. The lack of the degrading effect of the atmosphere compensates for the relatively small size of *HST*'s 2.4 m mirror.

The archive provides numerous data of different targets, with different filters and science goals. The ACS/WFC data provided by the Space Telescope Science Institute (STScI) are quite homogeneous in its format which allows us to build software that can apply a standard processing procedure for all data considered in this project. Most exposure times are ∼500 s in order to maximize the open shutter time. In addition, it is customary that longer observations be divided in a number of shorter exposures, allowing a median rejection of cosmic rays (CRs). Thus, typically three or more exposures of a field are obtained in sequence.

Access to the *HST*'s electronic archive is provided by the Multimission Archive at STScI (MAST[3]).

2.1. Field Selection

We considered observations obtained within 5° of the ecliptic, where the sky density of TNOs is highest, as their orbits are concentrated near the ecliptic (Brown 2001). Figure 1 shows the distribution of fields we considered.

It is common for ground-based surveys to prioritize fields located at opposition. This maximizes the parallactic motion with respect to the object's intrinsic velocity, allowing a reasonable 10%–20% uncertainty estimate on the distance if a circular orbit is assumed. It also permits a clear distinction of nearer, main belt asteroids from TNOs. Given the superior resolution of ACS/WFC data and the extra parallax derived from the motion of *HST* itself, it is not necessary to observe at opposition to constrain the distance to a moving object without having to rely on a circular orbit. For this reason, we did not restrict out attention to a specific range of solar elongation.

We consider images of the same field taken within the same *HST* orbit as part of a pointing. Only pointings that had a total open shutter time of over 1000 s with three or more images were considered. These images are typically taken within half an *HST* orbital period, ∼48 minutes. A total of 150 pointings were recognized as satisfactory for this project. We specifically excluded the many observations taken for the work by Bernstein et al. (2004), as those were previously searched for TNOs.

STScI makes available data in any step of the reduction process. We selected flat-fielded images that had not been undistorted or combined. We used the distortion corrections and PSF models for various filters provided by Anderson & King (2000). The filters that we considered for this work are summarized in Table 1.

2.2. Astrometric Solution

We search for solar system objects that change position between images over the time span of the pointing. The best astrometry possible is necessary to obtain a precise trajectory for TNOs. The astrometric accuracy provided by the archive's calibration is only as good as the astrometric precision of the *HST* guide star catalog provided for the "astrometric reference." However, the differential astrometry can be as accurate as the *HST*'s spatial resolution.

[3] http://archive.stsci.edu

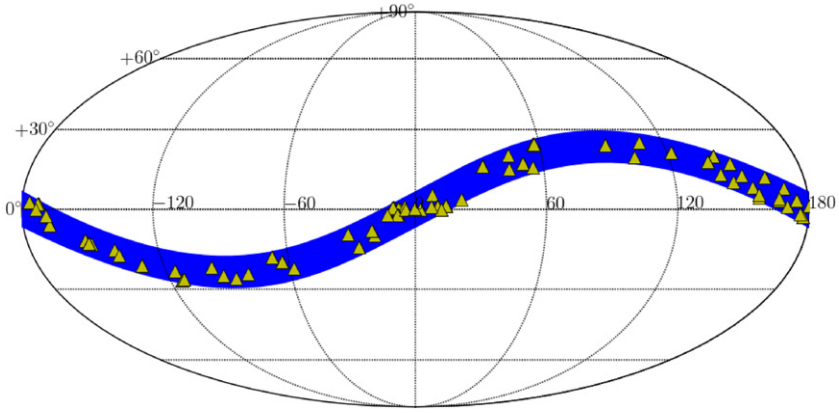

Figure 1. Map of the sky in J2000 coordinates. The 10°-wide ecliptic band we chose to select our pointings from is shown in blue. The location of all targets considered is plotted as yellow triangles. Many pointings are superimposed on top of each other.
(A color version of this figure is available in the online journal.)

Table 1
Photometric Conversion

Filter	Description	Zero Point	*R* Filter
F435W	Johnson *B*	25.17	−1.02
F475W	SDSS g'	25.77	−0.54
F555W	Johnson *V*	25.69	−0.66
F606W	Broad *V*	26.67	−0.61
F625W	SDSS r'	26.23	−1.03
F775W	SDSS i'	26.42	−0.65
F814W	Broad *I*	26.80	−0.69
F850LP	SDSS z'	25.95	+0.32

Notes. *HST* filter name, equivalent standard name, and their respective zero point. The transformation to *R* assumes TNO colors ($V - R = 0.6$, $R - I = 0.6$, $B - R = 1.6$).

Instead of combining data taken in different pointings, we took advantage of the precise differential astrometry between images obtained during the same orbit of the *HST*. ACS/WFC provides exquisite resolution (∼50 mas) and a stable and nearly constant PSF (Anderson & King 2000) across the field of view. There is, however, a significant large-scale distortion that needs to be accounted for before detections in different images can be compared with each other. In order to obtain a consistent astrometric solution for all the images in a single pointing, we used the distortion solution in the software developed by Anderson & King (2000) that considers filter-dependent distortions at the pixel level.

We defined the first image in the sequence as the "astrometric reference." All images were searched for sources and their positions transformed to the undistorted frame. All images in the pointing are registered to the reference by matching common sources. All detections are transformed to J2000 coordinates via the astrometric information in the reference image provided by STScI. In this way, there is a unique transformation from a detection in any image to J2000 coordinates. This transformation from the image array to sky coordinates is readily inverted to be used during the implanting of the control population, to be discussed in the next section. For static sources, the uncertainty in the position was very close to the 50 mas advertised by the ACS/WFC's documentation.

3. CONTROL POPULATION

Our moving object detection method requires the identification of an object in at least three different images. There are various reasons for an object in the field to go undetected. Being too faint is the most common. Chance alignment with a background star or CR will also reduce the chances of finding an object. Chip gaps and bad pixels should also be taken into account when considering the detection efficiency. We measure these and other unknown effects with the use of a control population that covers the range of observational characteristics the TNO population is expected to exhibit.

We implant our control population in the original flat-fielded images, before any distortion correction is applied. Since these objects go through the pipeline with the original data, anything that would affect our ability to detect real faint objects will also affect our ability to detect the objects that were implanted.

During the visual examination phase, to be discussed later, the operator is presented with thousands of candidate moving objects. This provides a constant stream of objects moving in TNO-like trajectories; real objects are indistinguishable from the control population. For the detection of new objects, the most important characteristics to be modeled are the brightness and rate of motion distribution for the synthetic population.

3.1. Apparent Motion

The control population also provides a test for the reduction pipeline, the recovery software, and the visual examination. The analysis pipeline, including the human interaction, will be successful if it discovers real objects that do not look special among the control population. This means the control population should be accurate and look like real TNOs. To avoid being biased toward finding exactly what we expect, based on what we already know about TNOs, we require a control population that spans all realistic properties (for example, orbits, colors, light curves, and binarity). However, for simplicity, we considered only single (not binary TNOs), showing no brightness variation in a ∼40 minute interval and with normal TNO colors (see Section 6.1). We only considered bound orbits.

In order to have both an accurate and inclusive TNO control population, we considered two different parameterizations. We first used the Keplerian orbital elements of an object to produce ephemerides. This allowed us to produce a distribution of orbital parameters similar to that of TNOs. The second one was based on the Bernstein & Khushalani (2000) elements which considers a Cartesian grid centered on the position of the observer at the time of observation. These elements are closely related to, and therefore a better measure of, the observational rates of motion. For this reason, this method is more inclusive. An equal

number of objects, usually 200, produced with each approach were implanted in each pointing. Ephemerides produced by these two methods using independent pieces of software, a variation of Bernstein & Khushalani (2000)'s *Orbfit*, and a custom made integrator, are used by the procedure that inserts synthetic objects in the original images.

3.2. Brightness Distribution

For any given pointing, we considered a uniform distribution in the instrumental magnitude. The faint end of this distribution was selected based on the reported instrumental zero point and exposure times of the images. We selected the magnitude distribution so that it would yield $\sim$ 50 detected objects per pointing, enough objects to sample the efficiency function of each field. The magnitude range spans 2.5 mag, and the faintest object was chosen to be half a magnitude fainter than the faintest object that should appear as a 1σ detection in an individual image.

As objects will trail over the course of an integration, our software computes the object's position at the beginning, middle, and end of the exposure based on its orbital parameters and the position of the *HST* at the time of the exposure. We fit a second-degree polynomial to this motion and then subdivide that motion in 1 pixel increments. We then divide the object's flux by the number of positions and insert a normalized PSF model at each position for that particular filter (Anderson & King 2000). Based on the position on the array, we can also correct the brightness of a source as another effect of the geometrical distortion. Since the photometric uncertainty of the objects that we are interested in is background-noise limited, no additional noise was added to trailed PSFs.

4. DETECTION OF MOVING OBJECTS

The usual strategy for finding TNOs that are detectable in single images relies in testing all correlations between detections across images that are consistent with a TNO orbit. From the ground, the image quality is such that exposure times of some minutes can be used before trailing is an issue. Then, we search for correlations between point-like sources that move from image to image. For observations taken over a single night of observation, the algorithm takes the list of detections and finds subsets that follow a straight line with a constant rate.

The diffraction-limited resolution with respect to the ground and the apparent motion induced by *HST* orbiting the Earth imply that TNOs detections will be trailed in typical exposure times (500 s). This trailing spreads an object's flux over a larger number of pixels, which for background-limited observations significantly decreases the likelihood of finding a faint moving object. For this project, we have taken a distinct approach that takes advantage of this apparent difficulty. Since all TNO detections will be trailed to some degree, analyzing a single set of detections (the centroid of the trails) is not the optimal method. This trailing motivates the overall strategy of our survey. We explore the range of orbital parameters consistent with the TNO region and keep those that produce significantly different trails, keeping them as test trails. Then, the search for sources in each image is optimized to select objects that show the particular test trail. Sources are then correlated in the same way ground-based observations are, and considering motion from image to image that is consistent with the test trail considered.

4.1. Detection Using Optimized Kernel Search

Searching for all possible orbits in the trans-Neptunian space requires an algorithm capable of sampling the complete set of observational features that real TNOs could exhibit. This usually translates into a set of possible rates in R.A. and Decl. that are surveyed with a rate resolution finer than that set by FWHM/Δt, where Δt is the time span of the observations. For *HST* data, this is a bit more complex than ground-based observations. The extra parallax due to the motion of *HST* around the Earth is $\sim$0.″4, significantly larger than the astrometric uncertainty (0.″05) implying some structure in a single detection can be identified even for TNOs.

This motivated us to use an optimized kernel search. Instead of taking the point-source catalog for every image and searching those for position correlations consistent with any orbit, we consider a set of orbits and search the images for detections consistent with them.

Each search is performed on the convolution of the original image and a kernel designed to match the signature of an object with the orbit being surveyed. This has the advantage of lowering the number of artifacts while increasing our sensitivity to moving objects. The use of kernels does not affect the photometry as it is only used for detecting sources. The kernels were computed on the fly in the same way a moving object is implanted, fitting a second-degree polynomial to its motion and implanting a set of 1 pixel separated PSFs on that track. The detection was performed using SExtractor (Bertin & Arnouts 1996) that has built in the use of kernels. The number of orbits considered depends on the kernels; if two orbits produce kernels that differ by less than a pixel in all images then only one is used.

For every orbit considered a catalog is generated and fed into our search algorithm. This takes the same set of orbital parameters used to create the kernel and constructs a shift matrix δ_{ij} that indicates by how much would an object with the current orbit in image i move from image j. Every detection in all images is considered as a possible moving object detection, and all other detections are tested for a possible link with it. Detections are linked by proximity to the putative new position using a threshold equivalent to the astrometric precision.

Only links of three or more detections are considered viable moving objects. We then filter solutions so that any detection belongs only to one possible moving object, using the astrometric error of the orbital solution with respect to the detections as the parameter to rank these links. The result is a list of candidate objects, each characterized by a set of detections.

4.2. Visual Examination

At this stage, the list of candidate objects is presented to a human operator to distinguish moving objects from spurious detections. Up to this point, the pipeline is fully automatic with no step in the reduction process requiring the input of an operator. The list produced is the pipeline's best guess for which detections appear to be related by a plausible orbit. However, no matter how efficient the processing might be, the whole pipeline relies on the positional information derived by SExtractor. It is nearly impossible to avoid chance alignment of spurious detections or poorly subtracted CRs, for example, and to program an automatic selection algorithm that could flag these events would be even harder.

The human brain is incredibly good at finding patterns. We make use of this fact by presenting the detections as a pattern recognition problem to a human operator. Each candidate is

represented by an animated postage stamp of the area around its location in the original image and the one that was CR-removed, both with the detections clearly marked. Both images are embedded in a Web site that gives the option of flagging the object as moving object or as an artifact. Information about the detections is also made available to the observer. It usually takes ∼3 minutes to a trained operator to flag all objects in a field as moving or artifact.

On average the operator is presented with ∼100 objects per pointing and nearly half of the detections that go through the human filter were recognized as artifacts. These usually correspond to: chance alignment of CRs (readily recognized due to their poor fit and for appearing much brighter than reported), extended objects elongated in the direction of the ecliptic (galaxies, saturated stars' wings), etc.

It is only now that the list of selected objects is compared to that of implanted ones. Those that are related to a synthetic object are used to characterize the detection efficiency of our method, and those that are "real" moving objects are flagged for constructing the luminosity function. In all pointings considered in this project, we recovered over 5000 fake objects, many times more than the 14 real objects discovered. The fact that real objects (apart from a binary) were indistinguishable from the implanted objects is a sign that the search is well described by our control population.

5. DETECTION EFFICIENCY

After the list of implanted objects is revealed and we correlate it with that of the objects found, the next step is computing the efficiency function. The likelihood of obtaining a particular set of objects from the control population depends on the efficiency function $\eta(R)$. This likelihood function $\mathcal{L}_\eta$ has the form

$$\mathcal{L}_\eta = \prod_{i=1}^{N^+} \eta(R_i) \times \prod_{j=1}^{N^-} \left[1 - \eta(R_j)\right], \quad (1)$$

$$\eta(R) = \frac{A}{2}\mathrm{erfc}\left[\frac{R - R_{50}}{2w}\right], \quad (2)$$

the probability of finding a set of objects $(1, \ldots, N^+)$ and of not finding the complement $(1, \ldots, N^-)$. The parameters in η are the maximum efficiency (A), the magnitude at which the detection probability equals half that of the maximum (R_{50}), and the width of the decline in probability (w). We search for those values that maximize $\mathcal{L}_\eta$.

In general, each pointing may be considered as an independent survey with its own detection efficiency and an area equal to ACS/WFC's field of view. However, this is only true for uncorrelated observations, where there is no chance of finding the same object in distinct pointings. Since we are using archival data, there are many consecutive observations of the same field that were included in our survey, where the probability of "discovering" an object twice is non-negligible. If this effect is not considered appropriately, we will overestimate the area surveyed and consequently underestimate the TNO luminosity function.

This problem may be solved if we know how many of the real TNOs would move from pointing to pointing. This requires that we have an accurate model for the orbital distribution of the TNO population, since different distributions will yield different levels of "contamination." The main variable determining how much an object appears to move is its distance to the observer. We used a distribution that resembles the heliocentric distribution in Fuentes & Holman (2008). The density of trial objects will determine the statistical significance of the overlapping areas between pointings.

We could use a single population with an accurate orbital distribution and a high density for the entire area of the sky. However, as the field of view of all our targets is negligible compared to the area from which they were selected a density of 10 per pointing would yield $\sim 10^8$ objects for which orbits and ephemeris would have to be computed. Additionally, a different control would be necessary to test the detection efficiency of uncommon, but physically plausible orbits.

Instead we chose to separate the problem into detection efficiency and effective area. The detection efficiency is well sampled for every pointing, as described above. In order to account for the area that was observed by more than one pointing we find all intersections between related pointings. The area that intersects two pointings corresponds to the fraction of the area in a field where a TNO could have been detected twice. Since we are dealing with moving objects, we need to take into account the orbit distribution of the real TNO population. We use a swarm of fake bodies in each pointing to estimate the overlap. We first identify plausibly correlated pointings by their observing time and location, 64 such sets were found. We then created a large population of mock orbits (1000) with similar characteristics to the real TNO population in each one of those pointings and computed how many fell in the field of view of each other. The result becomes a bit more complicated when we consider that an object could be in three or more of those pointings, each with its own efficiency function. In our survey, we had a maximum of five pointings that were correlated and could identify and precisely account for all intersection areas that were surveyed more than once. The effective area (Ω_{eff}) in Figure 4 has over 2000 parameters and was computed as shown in Equation (3):

$$\Omega_{\mathrm{eff}} = \sum_{i=1}^{N} \sum_{S \in \mathcal{P}_i} \Omega_S \eta_S, \quad (3)$$

$$\eta_S = 1 - \prod_{o \in S} (1 - \eta_o), \quad (4)$$

where the sum indexed i is carried out over all N sets of related pointings. If a set has n_i pointings, then there are 2^{n_i} possible combinations of overlapping fields or subsets S in its power set $\mathcal{P}_i$. Each one of those subsets represents an area Ω_S that was surveyed with a detection efficiency η_S. The detection efficiency of the subset is the probability of being detected in any of the pointings in it. The computation of Ω_S is provided by the fake bodies. It is the same fraction of a field's area as the fraction of objects created in any of the pointings in S that end up in all pointings in S.

Given the large number of fields and filters considered, and despite the many considerations the shape of the effective area does not vary too sharply compared to the total area and can be approximated as a function with only four parameters:

$$\Omega_{\mathrm{eff}}(R) \approx \frac{A}{4}\mathrm{erfc}\left[\frac{R - R_{25}}{2w_1}\right]\mathrm{erfc}\left[\frac{R - R_{25}}{2w_2}\right], \quad (5)$$

where the maximum effective area $A = 0.28 \pm 0.01\,\mathrm{deg}^2$, the magnitude at which the detection efficiency is 25% of its maximum $R_{25} = 26.5 \pm 0.1$, and the width of the decline in efficiency is parameterized as $w_1 = 0.78 \pm 0.3$ and $w_2 = 0.31 \pm 0.3$. In similar surveys, it is conventional to define the magnitude at which $\Omega_{\mathrm{eff}}(R)$ is half its maximum, which for our

Table 2
Found Objects

Name	MJD	R.A.	Decl.	Filter[a]	$\overline{m}$[a]	R	H	opp_ang (deg)	d[b] (AU)	i[b] (deg)
hst4	53318.1470775	11 : 06 : 02.741	3 : 12 : 09.186	F775W	25.7	25.0 ± 0.1	10.0	60.5	36.5 ± 1.4	2.9 ± 0.4
hst5[c]	53585.640178	22 : 15 : 01.360	−13 : 59 : 46.710	F814W	23.1	22.5 ± 0.3	6.8	160.9	42.9 ± 0.6	3.5 ± 0.2
hst6	53867.311035	22 : 38 : 46.527	−7 : 54 : 11.095	F814W	26.6	25.9 ± 0.3	10.3	73.1	41.5 ± 9.5	6.9 ± 4.5
hst7	53838.4348775	12 : 29 : 27.110	1 : 52 : 15.912	F850LP	25.4	25.7 ± 0.8	9.0	162.8	53.8 ± 1.9	62.7 ± 13.4
hst8	53964.9145558	3 : 21 : 46.568	16 : 52 : 34.607	F555W	26.7	26.1 ± 0.4	8.3	92.6	69.1 ± 33.3	14.7 ± 11.9
hst9	53956.060458	3 : 21 : 46.559	16 : 52 : 34.992	F814W	26.1	25.4 ± 0.2	11.5	84.2	28.2 ± 7.1	18.4 ± 16.4
hst10[d]	54034.98833	3 : 21 : 46.716	16 : 52 : 27.288	F625W	25.9	24.9 ± 0.3	6.5	160.9	79.0 ± 1.5	28.6 ± 21.4
							6.2		85.5 ± 3.3	105.5 ± 6.9
hst11	53786.0709287	12 : 13 : 50.319	2 : 48 : 43.607	F435W	23.6	22.6 ± 0.1	7.8	148.8	34.7 ± 2.5	4.9 ± 0.5
hst12	53989.5521546	0 : 39 : 18.864	0 : 53 : 11.789	F814W	26.6	25.9 ± 0.2	5.3	158.0	131.9 ± 4.5	93.1 ± 64.0
hst13[d]	53988.213526	0 : 39 : 34.385	0 : 51 : 40.193	F606W:F814W	25.9:25.9	25.3 ± 0.1	9.5	158.0	44.0 ± 1.9	8.4 ± 1.1
							8.4		56.2 ± 3.3	172.9 ± 2.0
hst14	54042.139279	9 : 47 : 03.493	10 : 06 : 25.987	F814W	25.9	25.3 ± 0.4	10.4	75.0	35.1 ± 1.0	33.6 ± 1.5
hst15	52764.837741	21 : 55 : 05.532	−9 : 22 : 01.181	F625W	25.3	24.2 ± 0.1	7.5	77.5	53.6 ± 1.7	3.5 ± 0.3
hst16[d]	52422.7726762	13 : 54 : 15.318	−12 : 33 : 23.226	F814W	25.6	24.9 ± 0.2	8.6	143.7	48.5 ± 1.4	2.6 ± 1.0
							7.9		57.6 ± 4.2	173.3 ± 6.3
hst17[e]	52941.37034	22 : 14 : 53.188	−14 : 00 : 40.282	F555W:F814W	25.8:25.8	25.1 ± 0.1	9.2	115.3	44.6 ± 2.5	9.4 ± 5.8

Notes. All objects found in this work are shown with their photometric and astrometric properties. Positions given for the first detections. The barycentric distance d and inclination i were estimated from an MCMC with a parameterization given by the *Orbfit* code (Bernstein & Khushalani 2000). Though some objects were discovered in the same field, the epoch of the observations is different. The solar system magnitude $H = V + 5 \log d\Delta$, a function of the V magnitude d and the distance to the observer Δ, is computed assuming that the phase angle is small and that the $V - R$ color for all objects is 0.6.

[a] When multiple filters are used, a filter list and corresponding instrumental magnitudes are shown.

[b] When prograde and retrograde solutions are possible, we report both peaks.

[c] This is the binary shown in Figure 3.

[d] The retrograde solution is presented in the second row; it is always at a larger distance from the observer than the prograde one.

[e] This object was found in two consecutive pointings. We found the same solution fitting both orbits, though we do not include the results of the second pointing as one of the detections is right on the edge of the detector.

survey is $R_{50} = 26.14$. The maximum effective area 0.28 deg^2 is comparable to the total area surveyed 0.45 deg^2. These differ due to the many fields that effectively sampled the same objects. The effective area is shown in the top panel of Figure 4.

After the real objects are recognized and some members of the control population are identified among the detected objects, we analyze the photometry and astrometry of each one of those detections. We construct the efficiency function and luminosity function. The orbital constraint on every object is also investigated to understand the uncertainties and possible degeneracies imposed by the data.

6. ANALYSIS

6.1. Photometry

After sources are detected, SExtractor (Bertin & Arnouts 1996) is used to obtain photometry. As was discussed in Section 2, TNOs will shift their position during the exposure and their shape will be elongated in the direction of motion. We selected the `AUTO` flux measurement since it is the most appropriate for extended objects. It uses an elliptical aperture which is computed for every detected source. Instrumental magnitudes are provided for each discovered object in Table 2.

For the range of magnitudes that is relevant for this study, the photometric uncertainty is dominated by the noise in the background illumination. This uncertainty is also computed by SExtractor and is in good agreement with the deviation between different images and with the error for implanted objects. The photometric accuracy depends mainly on the background brightness and the filter used.

The suite of filters that we considered for this project is presented in Table 1. Transformations between ACS/WFC magnitudes and UBVRI standard magnitudes were computed based on (Sirianni et al. 2005; Jordi et al. 2006) and considered typical colors for TNOs based on Doressoundiram et al. (2008) ($V - R = 0.6$, $R - I = 0.6$, $B - R = 1.6$).

6.2. Orbital Information

Though we use the position of the objects in each image and its trail over a single exposure to find orbits that are consistent with an objects' motion, we obtain a tighter constraint if we simulate the images themselves. We use the stability of *HST*'s PSF and its angular resolution to find the set of orbital parameters that are consistent with the data and in this way provide accurate uncertainty estimates for them.

Our ability to constrain the range of orbital parameters for a given object is greatly improved by the motion of the telescope during a pointing. The extra parallax and precise astrometry provided by *HST* allow us to better disentangle the parallactic and proper motion of an object during the exposure. The motion of *HST* will produce a parallax for any motion perpendicular to the ecliptic that will be evident as a curved path in the image. For fields at low ecliptic latitude, the component along the ecliptic is largest and changes with time, as the target "rises," "transits," and "sets" with respect to Earth throughout the pointing. On images with equal exposure time, this will manifest as a set of streaks with different lengths.

We run a Markov Chain Monte Carlo (MCMC) simulation where the function to minimize is the residual on the objects' image. To compute the χ^2, we consider a rectangular region around each detection that depends on the shape of the trail and the uncertainties in the data. We parameterize this function on variables related to the observed motion on the sky. We constrain

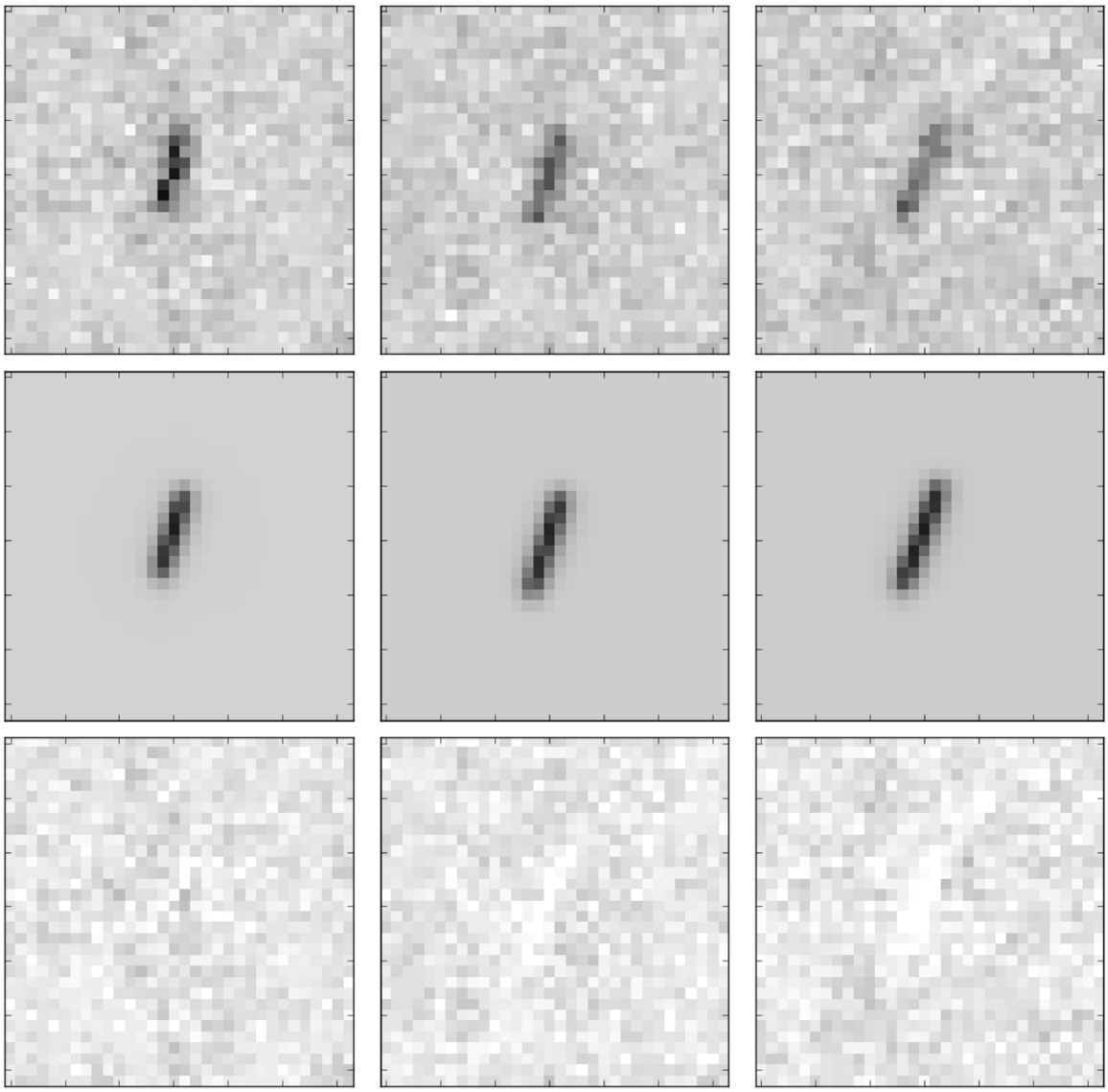

Figure 2. Images around the location of the found object hst11 in each of the three images in the pointing where it was found. Each row shows the data after CR processing, the model and the residuals for an acceptable trial sampled during the MCMC minimization of the residuals. Note that we did not fit for the fluxes but took them from SExtractor.

the number of parameters we fit for to those that affect the orbit of the objects, in order to speed the convergence of the Markov Chain, hence fluxes are taken from SExtractor. We use the best "test orbit" from the automatic process as the starting point to define the section of the images where the model and residuals will be computed. This allows the inclusion of all images in the pointing, regardless of whether SExtractor found the object in every image or of any error in the position of the detections.

The utility and success of MCMC is greatly increased if we are able to find a transformation to a set of orthogonal variables, where the effect on the target likelihood produced by a small change in one dimension is decoupled from changes in others. Using Keplerian elements is not the most appropriate choice of variables since a small change in one element would affect others if the position of the object at a given time is to remain constant, making our method very inefficient. For this part of the analysis, we considered the parameterization and routines developed by Bernstein & Khushalani (2000). These consider a Cartesian coordinate system centered on the observer that points toward the center of the first image. Though its variables are fairly independent when describing the parallactic motion of a TNO, we took into consideration a few modifications to the parameters. These changes of variable were chosen to ensure a smooth transition between different areas of the parameter space that yield similar trajectories. Since a change in distance also changes the travel time, we were forced to include a shift in the object's relative position in every step so that the Markov Chain would not get stuck updating all other parameters every time the distance changed.

The only constraint we imposed on trial orbits was that they were bound and that the velocity along the line of sight was zero, a good approximation given the short arc and the large distance to these objects. In Figure 2, we show the postage stamps around one of the objects, hst11, for an iteration in the Markov chain.

6.3. Binarity

In our sample of 14, there is only one object that is readily recognized as binary (see Figure 3). The separation between the components is $\delta\alpha = 0\farcs53 \pm 0.05$ and their magnitudes are: 23.6 ± 0.3 and 23.7 ± 0.3, respectively, making this a very likely equal-mass binary.

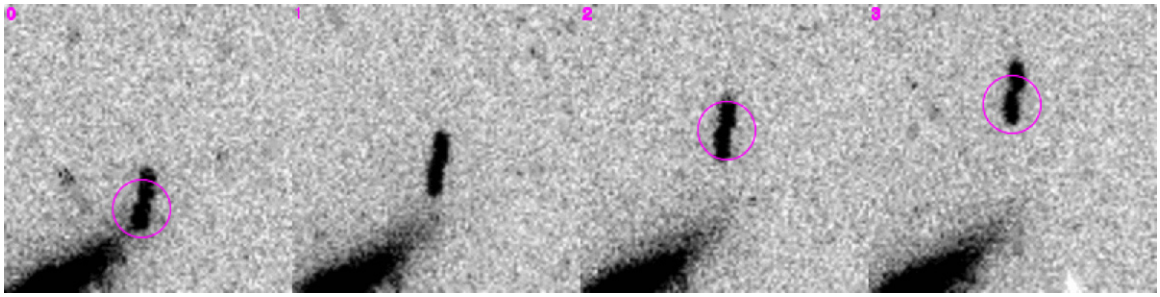

Figure 3. Postage stamp sequence of CR-corrected images around the position of hst5. No distortion correction has been applied to these images. The detections that were linked by the search algorithm are shown as magenta circles. The component closer to the background galaxy has an F814W magnitude of 23.6 ± 0.3 and the other one 23.7 ± 0.3. The separation is $\delta\alpha = 0\farcs53 \pm 0\farcs01$, which at a distance of 42.9 ± 0.6 AU gives a lower limit to their physical separation $a > 165,000 \pm 2000$ km. (A color version of this figure is available in the online journal.)

The characteristics of this binary are quite common among the binary TNO population. Its absolute solar system magnitude $H \sim 6.8$ (a proxy for size) and inclination ($i \sim 3.5$) place it among many other binaries in Noll et al. (2008, their Figure 2).

Figure 3 shows an obvious binary, however, limits on the binary fraction are difficult to obtain, given that we did not calibrate our search for binary detection. No binary control population was implanted and for this reason we are unaware of our efficiency at detecting them as a function of separation, brightness ratio, or orbit. Nevertheless, having one detection, we can only place a 7% lower limit on the fraction of wide, equal brightness binaries among the faint TNO population.

6.4. Size Distribution

Once the distance and magnitude are measured, we can compute the size of each body, assuming a value for the albedo. If we further assume that all objects are roughly at the same distance, the luminosity function can be written as a function of size, as shown in Figure 4 where we assume the distance $d = 42$ AU and the albedo $p = 0.07$ (Stansberry et al. 2008).

Introduced in Bernstein et al. (2004), the Double Power Law (DPL) is a handy functional form for the density of objects as a function of R magnitude that considers a break in the size distribution. The parameters are σ_{23} or the surface density of objects with $R = 23$, α_1 and α_2 or the slopes of the power-law behavior of the luminosity function for the brightest and smallest objects, and $R_{\rm eq}$ is the magnitude where the behavior changes from that of small to that of large sizes.

The previous best fit to the cumulative size distribution that combined the results of all surveys listed in Fuentes et al. (2009) is shown in Figure 4 in red. We also considered our 14 objects together with the many surveys that provide detailed information about their calibration (see Table 2 in Fuentes & Holman 2008; Fuentes et al. 2009; Fraser & Kavelaars 2009). The total area surveyed or effective area in all those surveys is plotted in the top panel of Figure 5. We consider only objects that were discovered at magnitudes brighter than the magnitude at which their respective surveys' detection efficiency fell below 15% of the maximum efficiency.

Using the orbital information provided in those surveys, we define the hot and cold populations as those with inclinations larger and smaller than 5°. A caveat about some of the surveys that provide inclination and distance information with a ~24 hr arc at opposition is that they can only compute a rate of motion on the sky. Fuentes et al. (2009) included only the rate of motion for every object, from which we computed the distance and inclination.

We analyzed the likelihood function for all these observations given the effective surveyed area following the MCMC analysis described in Fuentes & Holman (2008). The likelihood function is plot against two of the DPL variables in each of the panels in Figure 8 for the hot, cold, and all objects (top, middle, and lower panel, respectively). The constraints on the DPL parameters computed on the likelihood of each parameter marginalized over all others are: $\alpha_1 = 0.89 \pm 0.10$, $\alpha_2 = 0.29 \pm 0.06$, $\Sigma_{23} = 1.61 \pm 0.11$, $R_{\rm eq} = 23.8 \pm 0.3$ for all objects considered, $\alpha_1 = 0.70 \pm 0.10$, $\alpha_2 = 0.30 \pm 0.07$, $\Sigma_{23} = 0.93 \pm 0.03$, $R_{\rm eq} = 24.1 \pm 0.7$ for hot objects, and $\alpha_1 = 0.80 \pm 0.08$, $\alpha_2 = 0.21 \pm 0.09$, $\Sigma_{23} = 0.92 \pm 0.02$, $R_{\rm eq} = 24.2 \pm 0.4$ for cold ones.

7. DISCUSSION

Our search can be compared to the targeted use of *HST* by Bernstein et al. (2004) where six fields were imaged ~20 times each to find the faintest TNOs possible. Though that search was significantly more sensitive to faint objects due to a careful selection of the fields, the co-addition of signal and the use of a wide-filter, it only focused on six independent fields. That group found three objects, two of which remain the faintest TNOs ever imaged. This work would have been able to detect the two brightest of those objects in any pointing that satisfied our criteria. A more targeted survey, with better selection of filters and pointings at the stationary point, where objects would not trail as much, would be much more efficient at finding TNOs than our archival search.

Of the total area imaged, 0.45 deg^2 corresponding to the 150 pointings that were analyzed, the effective area for this survey is only 0.3 deg^2, as shown in the top panel of Figure 4. This is due to background sources, CR confusion, and any other feature that would completely or partially prevent us from detecting an object in at least three images. The main cause for this reduced survey area is, however, the existence of pointings of the same field taken in succession, which effectively increases the chances of detecting an object in that field but decreases the area of our survey by re-observing a field, where the same objects are visible, many times.

The luminosity function of the 14 objects discovered in this survey is presented in the lower panel of Figure 4. The effective area is also plotted in the top panel to put the significance of each detection in context. The previous best fit to the TNO population is plotted in green, the best fit for all surveys (including this ones) is also plotted in red. As we can see, our survey follows precisely the expectations derived from the previous work. There are two bright objects $R < 23$ among the 14, which indicate a

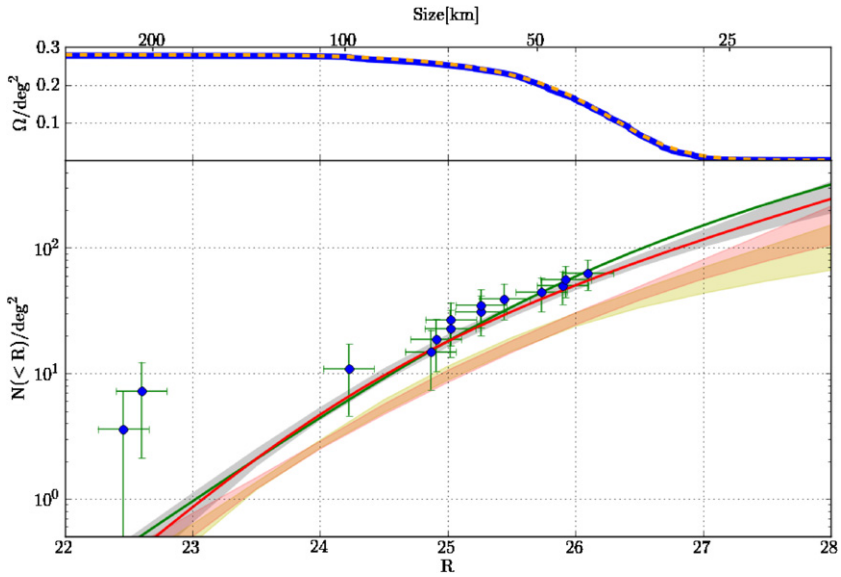

Figure 4. Top panel shows the effective area surveyed in this paper as a function of R magnitude in blue. While that function depends on the efficiency function and shared area of every pointing in this survey, we can simplify the ∼2000 parameters (see Equation (3)) into the four parameters of the function plot in dashed orange (see Equation (5)). The lower panel shows the luminosity function of objects found in this survey, normalized by the effective area at each magnitude. The best model in Fuentes et al. (2009) is overplotted in green, while the best model for all surveys, including this one, is shown in red. The gray area represents the area enclosed by the 1σ confidence region for all surveys. The lower set of shaded areas represents the 1σ confidence limits for the cumulative function of the hot (red) and cold (yellow) populations.

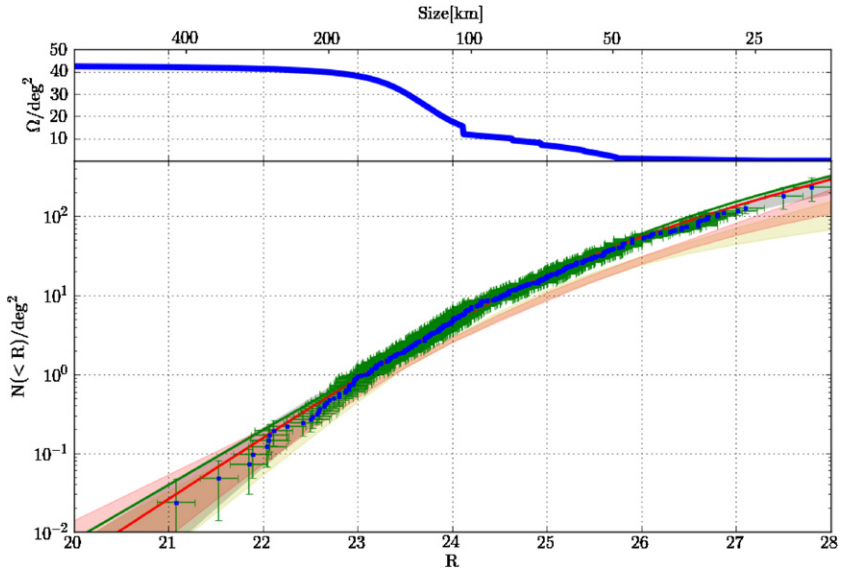

Figure 5. Top panel shows in blue the effective area for all surveys considered in this paper as a function of R magnitude, normalized by the effective area at each magnitude. The lower panel shows the luminosity function of TNOs in all surveys considered, normalized by the effective area at each magnitude. The best model in Fuentes et al. (2009) is overplotted in green, while the best model for all surveys, including this one, is shown in red. The gray area corresponds to the 1σ confidence region given for all objects. The same confidence regions are given for hot and cold objects, in red and yellow, respectively.

higher density than expected. The statistical significance of this deviation is low.

We took most calibrated surveys for TNOs in the literature (see Section 6.4), along with this one, to construct an effective survey area and luminosity function for all these objects, shown in Figure 5. There are over 400 TNOs included, which allow a precise constraint on the luminosity function. The two faintest objects beyond $R = 27.5$ were discovered with *HST* (Bernstein et al. 2004), and we see that ground-based surveys are already sensitive to $R = 27$ TNOs.

The exquisite astrometric precision in *HST* data enables us to measure a TNO's distance and inclination with a few percent uncertainty, even from an arc as short as 40 minutes. Although an object's motion depends on the solar elongation at which the observations were taken, the extra motion due to *HST*'s orbit helps disentangle the objects' parallax from its proper motion along the ecliptic. Though this is a sample of only 14 objects, the distances found are in good agreement with Kavelaars et al. (2008). Dynamically, cold objects are constrained to $35 < \mathrm{d} < 50$ AU, while hot objects do not cluster at a particular distance (see Table 2).

Using the inclination information in Table 2, we separate objects into the hot and cold dynamical classes, for this we use a simple $i = 5^\circ$ cutoff. Applying this filter to all surveys, we compute the luminosity function of hot and cold objects (shown in Figure 6 and Figure 7, respectively). We see that the bright-

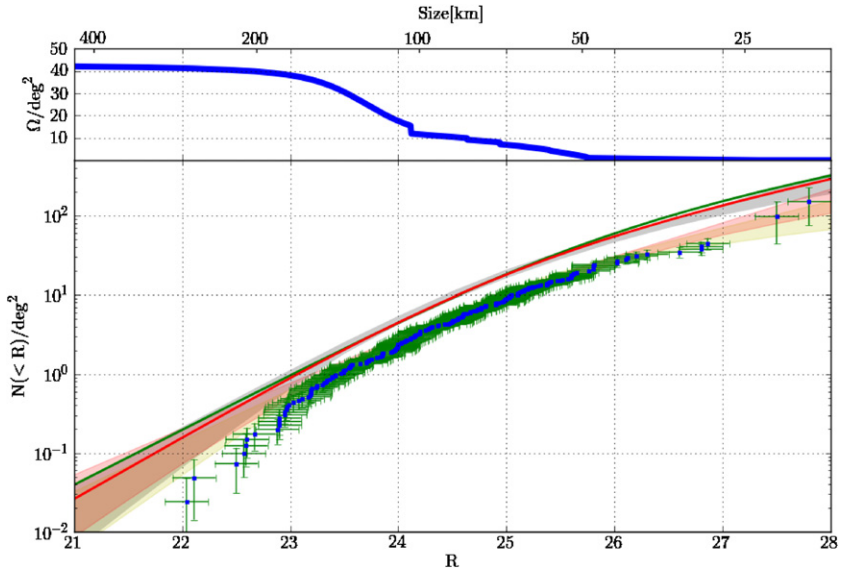

Figure 6. Same as Figure 5 but only for objects deemed dynamically cold, $i \leqslant 5^{\circ}$.

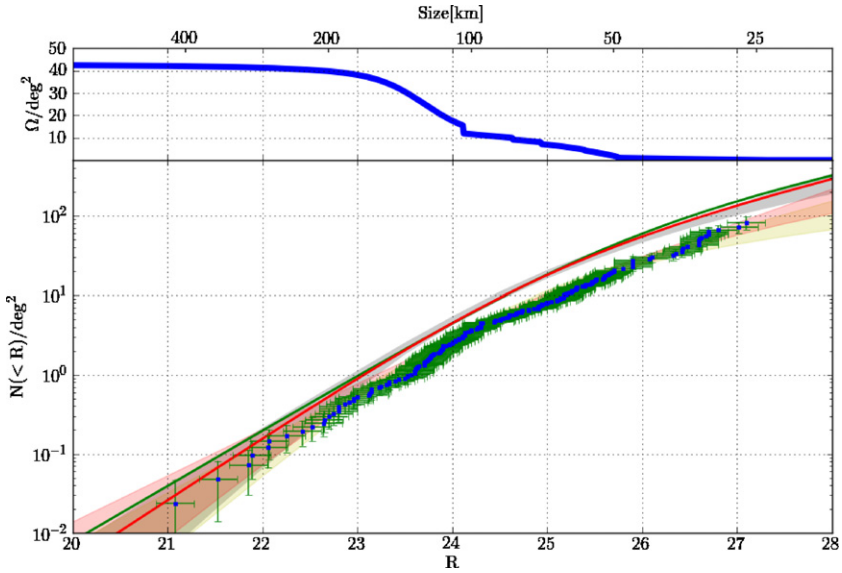

Figure 7. Same as Figure 5 but only for objects deemed dynamically hot, $i > 5^{\circ}$.

end and faint-end slopes for the hot and cold populations are similar. This is best seen in the MCMC posterior probability for the luminosity function DPL parameters (see Figure 8). The hot and cold luminosity function constraints on α_2, the faint-end slope, are consistent with each other. However, there is a significant deviation at the bright end of the dynamical hot population between the best-fit model and the luminosity function which indicates that the size distribution of bright hot objects is shallower than that of the cold fraction, the largest and brightest objects tend to be dynamically excited, consistent with the results of Levison & Stern (2001) and Bernstein et al. (2004). Our lack of data to constrain the bright end of the TNO luminosity function is explained as most of the objects in our analysis come from well-characterized pencil beam surveys where only a few large objects are present. For the same reason, our constraints are more significant for the faint end of the luminosity function.

This result is in contradiction with claims that the luminosity function of hot and cold objects differs for small bodies (Bernstein et al. 2004; Fuentes & Holman 2008). However, there is an explanation for this difference. For a long time, the only TNOs fainter than $R \sim 26$ were those found by Bernstein et al. (2004), all of them cold. This lack of faint hot objects allowed for extremely flat slopes for smaller sizes. By including the deeper surveys of Fuentes et al. (2009) and Fraser & Kavelaars (2009), which have detected several high inclination objects, the non-detection of $R > 27$ hot objects is less significant.

However, these deep ground-based surveys rely on short arcs and must constrain their orbits to be circular to compute a distance and inclination. This increases the probability of contamination between hot and cold objects. This problem is less severe with detections obtained from *HST*. In our survey, we see roughly equal number of cold and hot objects, which is consistent with the ground-based inclinations being accurate.

As was discussed earlier, the size distribution is intimately related to the luminosity function. If we disregard the distance estimate and assume all objects are located at 42 AU and have a 7% albedo, the transformation is direct and corresponds to the top axis in Figure 5. The break magnitude that marks the transition between the bright and the faint slope luminosity

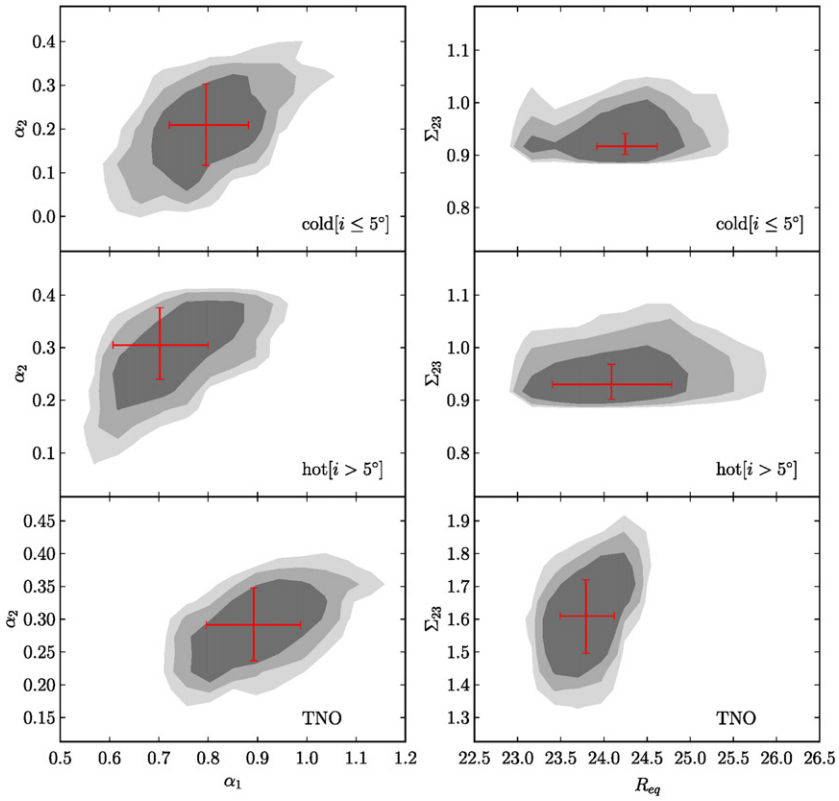

Figure 8. Probability density for the surface number density $\sigma(R)$. The parameters are those in the DPL model. In each panel, the painted areas represent the 3σ, 2σ, and 1σ confidence regions. The panels on the left show the probability distribution as a function of the power-law exponents for bright and faint objects (α_1, α_2). Panels on the right axis show the likelihood of the brightness at which the luminosity function changes slope ($R_{\rm eq}$) and the density of objects at $R = 23$ (Σ_{23}). The red crosses show the 1σ confidence region for each parameter when the probability density has been marginalized over all other variables. The details of this likelihood analysis can be found in Fuentes & Holman (2008) and references therein. The bottom panel shows the results for all objects in all surveys considered, the most likely value for the parameters is: $\alpha_1 = 0.89 \pm 0.10$, $\alpha_2 = 0.29 \pm 0.06$, $\Sigma_{23} = 1.61 \pm 0.11$, and $R_{\rm eq} = 23.8 \pm 0.3$. The middle panel shows only objects considered as hot or excited, selected for having $i > 5°$, the best parameters are: $\alpha_1 = 0.70 \pm 0.10$, $\alpha_2 = 0.30 \pm 0.07$, $\Sigma_{23} = 0.93 \pm 0.03$, and $R_{\rm eq} = 24.1 \pm 0.7$. The top panel corresponds to cold objects ($i \leqslant 5°$), where the most likely solution is $\alpha_1 = 0.80 \pm 0.08$, $\alpha_2 = 0.21 \pm 0.09$, $\Sigma_{23} = 0.92 \pm 0.02$, and $R_{\rm eq} = 24.2 \pm 0.4$.

(A color version of this figure is available in the online journal.)

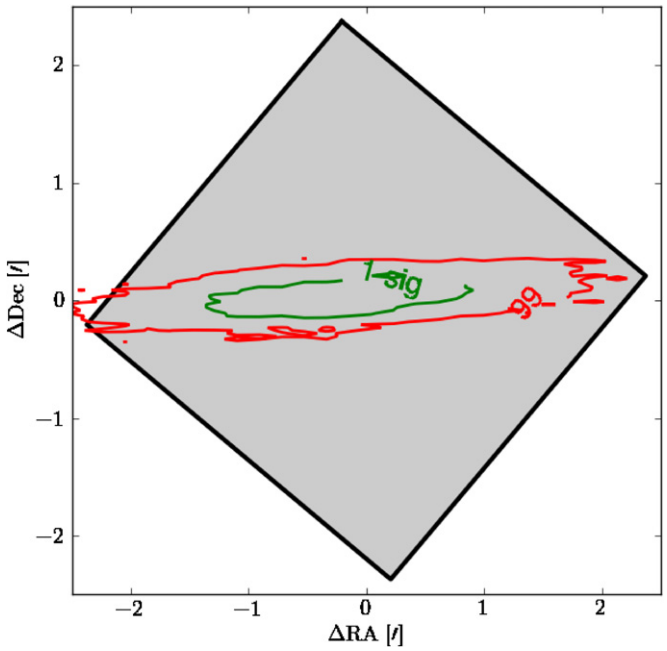

Figure 9. 1σ (green) and 99% (red) uncertainty in the position of a particular object (120° solar elongation), 30 days after discovery. The field of view of ACS/WFC is overplotted as a black square.

(A color version of this figure is available in the online journal.)

function becomes then a break in the size distribution. Such a break is expected from the collisional evolution the TNO population has undergone since these objects formed (Kenyon & Bromley 2004; Kenyon et al. 2008; Pan & Sari 2005). We find the location of such break to be consistent for both hot and cold populations $D_{\rm eq} \sim 100$ km. In the model of Pan & Sari (2005), such a large size corresponds to the largest object that has been disrupted in the age of the solar system. We note that this result relies on an assumed distance and albedo for all objects, something that we know is inaccurate for distances. The albedo is also likely to be different as there seems to be a correlation with size and color (Stansberry et al. 2008).

The results discussed in this section constrain the TNO size distribution at low ecliptic latitudes. As we cover more of the sky, sampling the TNO population away from the ecliptic we will measure density of objects as a function of latitude, as well as the relative proportion of hot versus cold objects. We shall be able to include more objects in our analysis and hence put better constraints on the location of the break in the size distribution, for different dynamical families.

Among the objects found, there is a wide-separation binary. Since we did not consider the possibility of binaries in our control population, we cannot directly extract the statistical significance of our measurement. However, our result allows us to set a limit on the binary fraction of 7^{+13}_{-2}%, in excellent

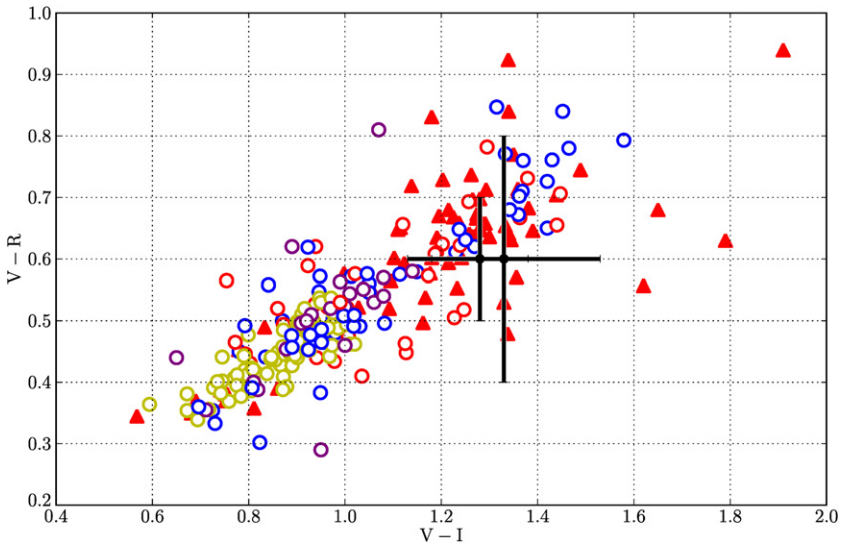

Figure 10. Colors for our two objects along with previously known TNOs in the mboss database (Hainaut & Delsanti 2002). (Red triangles: classicals; in circles, red: plutinos; blue: scattered and centaurs; yellow: trojans; purple: long- and short-period comets.) The black points correspond to hst13 and hst17, respectively, where the $V-R$ color for both is assumed to be 0.6 and the uncertainties are the same as those in $V-I$.

(A color version of this figure is available in the online journal.)

agreement with the current limits for different population of 5%–20% (Noll et al. 2008).

The objects presented in this paper typically cannot be followed up. The short observation arc and the long time elapsed since the date the observations were taken imply an uncertainty in the position too large to recover in current observations. However, the orbital estimates are accurate enough to grant an uncertainty ellipse that fits within an ACS/WFC fields within a month after the discovery observation (see Figure 9). This opens the possibility of a slightly different observing strategy, where data are processed as they become available, and follow-up observations can be scheduled quickly.

For the couple of objects with two different filter observations, we put them in the context of the Hainaut & Delsanti (2002) database, as shown in Figure 10. The two objects seem to fall right where expected for classicals, which is consistent with their inclination estimates: $i \sim 10^\circ$ and 5°. For at least these two objects, the assumption $V - R = 0.6$ is justified.

8. CONCLUSIONS

We have successfully completed a search for TNOs within 5° of the ecliptic using archival data taken with the ACS/WFC camera aboard *HST*. The data span six years. Of the 150 pointings analyzed 14 objects were found, yielding roughly 1 object per 10 pointings. This suggests that there are possibly hundreds of new TNOs with exquisite astrometry and photometry still hidden in the ACS/WFC archive at higher ecliptic latitudes. We have proven our ability to detect and characterize these even with data intended for completely different purposes, where most of the filters and strategies used for these observations are sub-optimal for detecting TNOs.

Given the excellent astrometric precision of the images, it is possible to use observations taken in a single pointing of *HST* to predict the position of a TNO a month later and have the uncertainty ellipse fit within the field of view of ACS. This, coupled to the fast turnover of data from our pipeline, may yield many viable candidates for follow-up observations. A detection a month later would allow us to collect a significant set of small TNOs with accurate orbits, opening the possibility for detailed observations with present and future instruments like the *James Webb Space Telescope*.

Binaries are only detected as such if the separation of the components on the plane of the sky can be resolved. The trailing of the binary imposes further constraints to the fraction of time a given binary would be recognized, which is specially problematic for *HST* data where trailing of TNOs is more prominent. Previous searches for binaries using *HST* have surveyed known TNOs and tracked the telescope to counteract their motion. The one relatively faint ($R \sim 23$) binary discovered in this project illustrates the successful detection of a trailed binary. This opens the possibility of constraining the rate of binaries as a function of size from the same survey in which the TNOs are discovered.

The recognition of a low and high inclination population among TNOs (Brown 2001) has been interpreted as the existence of two dynamically distinct set of objects. Those with higher inclinations or excited (hot) and those with lower inclinations and not excited (cold). Bernstein et al. (2004) found that these two defined by their inclination had different size distributions. There is also evidence that they have different colors (Doressoundiram et al. 2008).

The cold population's size distribution is steeper than that of the hot population for objects larger than ∼100 km (Levison & Stern 2001). In this paper, we show that the location of the break in the size distribution and its slope for objects fainter than it for cold and hot objects are consistent with each other. This is compatible with the theory of collisional evolution, where a population with a given steep power-law size distribution gets collisionally grinded as time progresses (Pan & Sari 2005; Kenyon & Bromley 2004; Kenyon et al. 2008). The slope of the size distribution of small objects in those models is constant since it is given by the steady state of collisions. The location of the break is also consistent for both populations, but $D_{\rm eq} \sim 100$ km is larger than what theories expect.

This difference could be better understood if any albedo dependence with size is first investigated for smaller objects. At present, we can only extrapolate the apparent correlations between size and color, and inclination and albedo from measurements performed only on the largest, brightest TNOs. By

chance, multifilter observations of two TNOs were obtained, yielding $V-I$ colors for two objects. We expect to find more of these serendipitous color observations for other faint TNOs in intensively surveyed fields away from the ecliptic.

The advent of the Wide Field Camera 3 installed in 2009 May opens the possibility for extending this work to the near-IR and to a larger fraction of the data collected by *HST*. The prospects of such observations would allow extending surface studies to small objects.

As we continue the analysis of *HST* archival data to higher ecliptic latitudes, we will start sampling an area of the sky that has only been surveyed for brighter ($R \lesssim 21$; Trujillo & Brown 2003). When the whole archive is searched, we shall take the depth and resolution of pencil beam searches to the whole sky.

Support for program 11778 was provided by NASA through a grant from the Space Telescope Science Institute, which is operated by the Association of Universities for Research in Astronomy, Inc., under NASA contract NAS 5-26555.

REFERENCES

Allen, R. L., Bernstein, G. M., & Malhotra, R. 2002, AJ, 124, 2949
Anderson, J., & King, I. R. 2000, PASP, 112, 1360
Bernstein, G., & Khushalani, B. 2000, AJ, 120, 3323
Bernstein, G. M., Trilling, D. E., Allen, R. L., Brown, M. E., Holman, M., & Malhotra, R. 2004, AJ, 128, 1364
Bertin, E., & Arnouts, S. 1996, A&AS, 117, 393
Brown, M. E. 2001, AJ, 121, 2804
Brown, M. E. 2008, in The Solar System Bayond Neptune, ed. M. A. Barucci et al. (Tucson, AZ: Univ. Arizona Press), 335
Brucker, M. J., Grundy, W. M., Stansberry, J. A., Spencer, J. R., Sheppard, S. S., Chiang, E. I., & Buie, M. W. 2009, Icarus, 201, 284
Chiang, E. I., & Brown, M. E. 1999, AJ, 118, 1411
Doressoundiram, A., Boehnhardt, H., Tegler, S. C., & Trujillo, C. 2008, in The Solar System Bayond Neptune, ed. M. A. Barucci et al. (Tucson, AZ: Univ. Arizona Press), 91
Fraser, W. C., & Kavelaars, J. J. 2009, AJ, 137, 72
Fraser, W. C., et al. 2008, Icarus, 195, 827
Fuentes, C. I., George, M. R., & Holman, M. J. 2009, ApJ, 696, 91
Fuentes, C. I., & Holman, M. J. 2008, AJ, 136, 83
Gladman, B., Kavelaars, J. J., Petit, J.-M., Morbidelli, A., Holman, M. J., & Loredo, T. 2001, AJ, 122, 1051
Hainaut, O. R., & Delsanti, A. C. 2002, A&A, 389, 641
Jordi, K., Grebel, E. K., & Ammon, K. 2006, A&A, 460, 339
Kavelaars, J., Jones, L., Gladman, B., Parker, J. W., & Petit, J. 2008, in The Solar System Bayond Neptune, ed. M. A. Barucci et al. (Tucson, AZ: Univ. Arizona Press), 59
Kenyon, S. J., & Bromley, B. C. 2004, AJ, 128, 1916
Kenyon, S. J., Bromley, B. C., O'Brien, D. P., & Davis, D. R. 2008, in The Solar System Beyond Neptune, ed. M. A. Barucci et al. (Tucson, AZ: Univ. Arizona Press), 293
Levison, H. F., & Stern, S. A. 2001, AJ, 121, 1730
Morbidelli, A., Levison, H. F., & Gomes, R. 2008, in The Solar System Bayond Neptune, ed. M. A. Barucci et al. (Tucson, AZ: Univ. Arizona Press), 275
Noll, K. S., Grundy, W. M., Chiang, E. I., Margot, J., & Kern, S. D. 2008, in The Solar System Bayond Neptune, ed. M. A. Barucci et al. (Tucson, AZ: Univ. Arizona Press), 345
Pan, M., & Sari, R. 2005, Icarus, 173, 342
Petit, J.-M., Holman, M. J., Gladman, B. J., Kavelaars, J. J., Scholl, H., & Loredo, T. J. 2006, MNRAS, 365, 429
Sirianni, M., et al. 2005, PASP, 117, 1049
Stansberry, J., Grundy, W., Brown, M., Cruikshank, D., Spencer, J., Trilling, D., & Margot, J.-L. 2008, in The Solar System Beyond Neptune, ed. M. A. Barucci et al. (Tucson, AZ: Univ. Arizona Press), 161
Trujillo, C. A., & Brown, M. E. 2003, Earth Moon Planets, 92, 99